

Supporting Information

Unique 3D Heterojunction Photoanode Design to Harness Charge Transfer for Efficient and Stable Photoelectrochemical Water Splitting

Jungang Hou,^{ab*} Huijie Cheng,^a Osamu Takeda,^b Hongmin Zhu^{ab*}

^aSchool of Metallurgical and Ecological Engineering, University of Science and Technology Beijing,

Beijing 100083, China

^bTohoku University, 6-6-02 Aramaki-Aza-Aoba, Aoba-ku, Sendai, 980-8579 Japan

Corresponding author: jhou@ustb.edu.cn; hzhu@material.tohoku.ac.jp

Captions of Supporting Information

Figure S1. Photoelectrochemical water splitting reactor. (1) working electrode; (2) counter electrode (Pt); (3) reference electrode; (4) electrochemical work station; (5) computer; and (6) Xe lamp.

Figure S2. Schematic sketch of various-dimensional TaON arrays prepared the hydrothermal induced self-assembly technique with the increasing concentration of HF solution ($M1 < M2 < M3 < M4$).

Figure S3. Typical magnified top-view scanning electron microscopy images of the nanorods-assembled TaON nanostructured array.

Figure S4. Typical magnified top-view scanning electron microscopy images of the nanorods-assembled TaON nanostructured array with a little content of nanosheets.

Figure S5. Typical magnified top-view scanning electron microscopy images of the 1D/2D nanorod/nanosheet-assembled TaON nanostructured array.

Figure S6. Typical magnified top-view scanning electron microscopy images of the one-dimensional spindle-assembled TaON nanostructured array.

Figure S7. Typical top-view scanning electron microscopy images of the 1D/2D nanorod/nanosheet-assembled TaON nanostructured array with the high yields.

Figure S8. Ba 2p of X-ray photoelectron spectra of the 1D/2D nanorod/nanosheet-assembled Ba-TaON nanostructured array.

Figure S9. Energy-dispersive X-ray spectra of the $\text{CoO}_x/\text{C}_3\text{N}_4/\text{Ba-TaON}$ heterostructured array.

Figure S10. Energy-dispersive X-ray spectra of the $\text{CoO}_x/\text{C}_3\text{N}_4/\text{Ba-TaON}$ heterostructured array. EDS analyses of 1D/2D nanorod/nanosheet-assembled Ba-TaON. (a) Co, (b) Ba, (c) N, (d) C, (e) O, (f) Ta, respectively. The elemental mapping revealed uniform distribution

of Co, C, N, O, Ba, Ta elements of the $\text{CoO}_x/\text{C}_3\text{N}_4/\text{Ba-TaON}$ sample.

Figure S11. XRD patterns of the different photoanodes. (i) Ba-TaON, (ii) $\text{C}_3\text{N}_4/\text{Ba-TaON}$ and (iii) $\text{CoO}_x/\text{C}_3\text{N}_4/\text{Ba-TaON}$ arrays.

Figure S12. (a) XRD patterns of tantalum-based arrays with various nitridation temperature : (i) without nitridation, (ii) 650 °C, (iii) 700 °C and (iv) 750 °C. (b) Ta 4f XPS spectra of (i) TaON, (ii) $\text{C}_3\text{N}_4/\text{TaON}$ and (iii) $\text{CoO}_x/\text{C}_3\text{N}_4/\text{TaON}$.

Figure S13. Ta 4f X-ray photoelectron spectra of (i) TaON, (ii) $\text{C}_3\text{N}_4/\text{TaON}$ and (iii) $\text{CoO}_x/\text{C}_3\text{N}_4/\text{TaON}$.

Figure S14. Raman spectra of $\text{CoO}_x/\text{C}_3\text{N}_4/\text{TaON}$ heterostructured array.

Figure S15. Photocurrent–potential curves under AM 1.5G-simulated sunlight of TaON photoanode under the nitridation of 650~750 °C.

Figure S16. I-V curves of the photoelectrodes of the undoped and Ba-doped TaON arrays. Bottom-right inset shows the schematic drawing of the structure for I-V measurement. Indium thin film was evaporated on the surface through a shadow mask as top electrode.

Figure S17. Mott–Schottky plots of TaON and barium-doped TaON photoelectrodes in 1.0 M NaOH solution (pH = 13.6) under the frequency of 3000 Hz.

Figure S18. Transient photocurrent density versus time in 1 M NaOH solution of pH=13.6 under AM 1.5G irradiation at 1.23 V versus RHE for the different photoanodes. (i) Ba-TaON, (ii) $\text{C}_3\text{N}_4/\text{Ba-TaON}$ and (iii) $\text{CoO}_x/\text{C}_3\text{N}_4/\text{Ba-TaON}$ arrays.

Figure S19. Photocurrent–potential curves under AM 1.5G-simulated sunlight of the hierarchical Ba-TaON, $\text{C}_3\text{N}_4/\text{Ba-TaON}$ and $\text{CoO}_x/\text{C}_3\text{N}_4/\text{Ba-TaON}$ photoanode with H_2O_2 as a hole-scavenging electrolyte under AM 1.5G simulated sunlight (100 mW/cm²).

1. Experimental section.

Fabrication of C₃N₄ nanosheet

First, bulk C₃N₄ was synthesized by directly heating low-cost melamine based on the previous work.¹ In detail, 5 g of melamine powder was put into an alumina crucible with a cover, then heated to 500 °C in a muffle furnace for 4 h at a heating rate of 20 °C/min to obtain the bulk C₃N₄. Next, 30 mg of bulk C₃N₄ was dispersed in 100 mL isopropyl alcohol at room temperature and exfoliated by ultrasonication for 12 h. The resultant dispersions were centrifuged at 3000 rpm for 10 min. After centrifugation, the supernatant (exfoliated C₃N₄ nanosheets, about top five sixths of the centrifuged dispersion) was collected by pipette. The mass remaining in the supernatant was estimated by drying and weighing the sediments in the centrifugal tube and about one third of the starting material remained in the supernatant. Namely, the exfoliated C₃N₄ nanosheets were obtained.

References.

1. S. C. Yan, Z. S. Li, Z. G. Zou, *Langmuir*, 2009, 25, 10397.

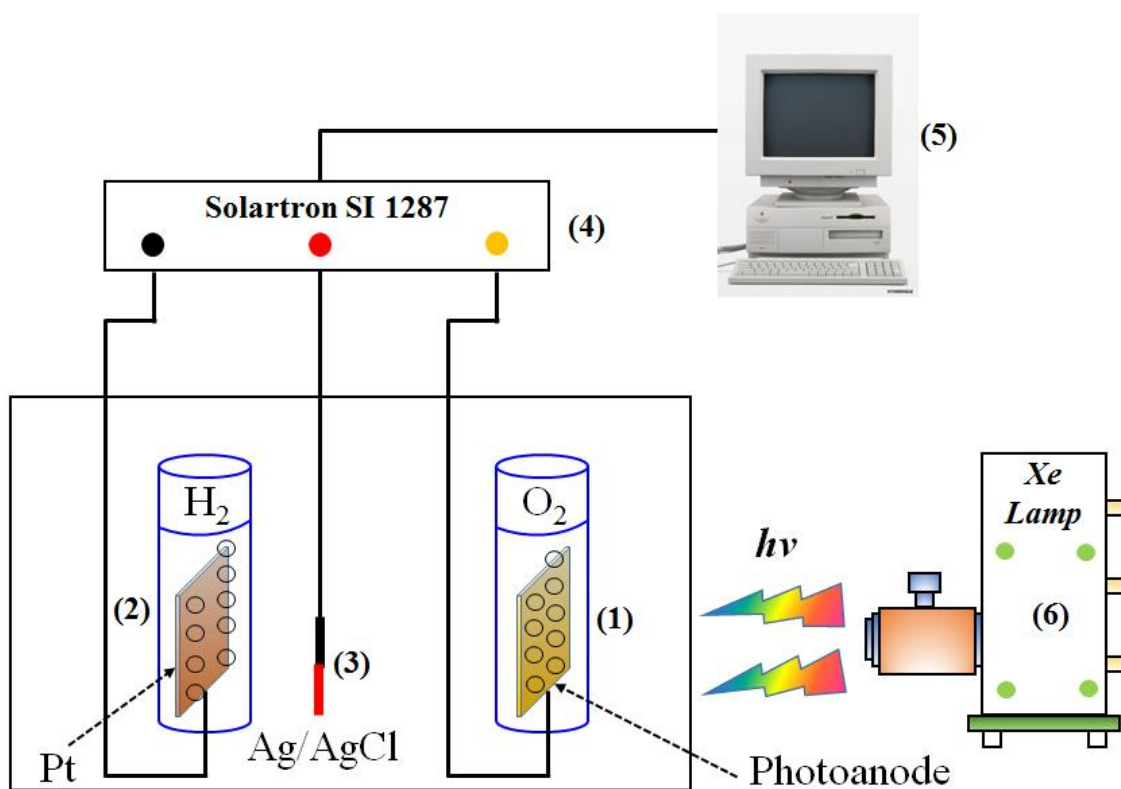


Figure S1. Photoelectrochemical water splitting reactor. (1) working electrode; (2) counter electrode (Pt); (3) reference electrode; (4) electrochemical workstation; (5) computer; and (6) Xe lamp.

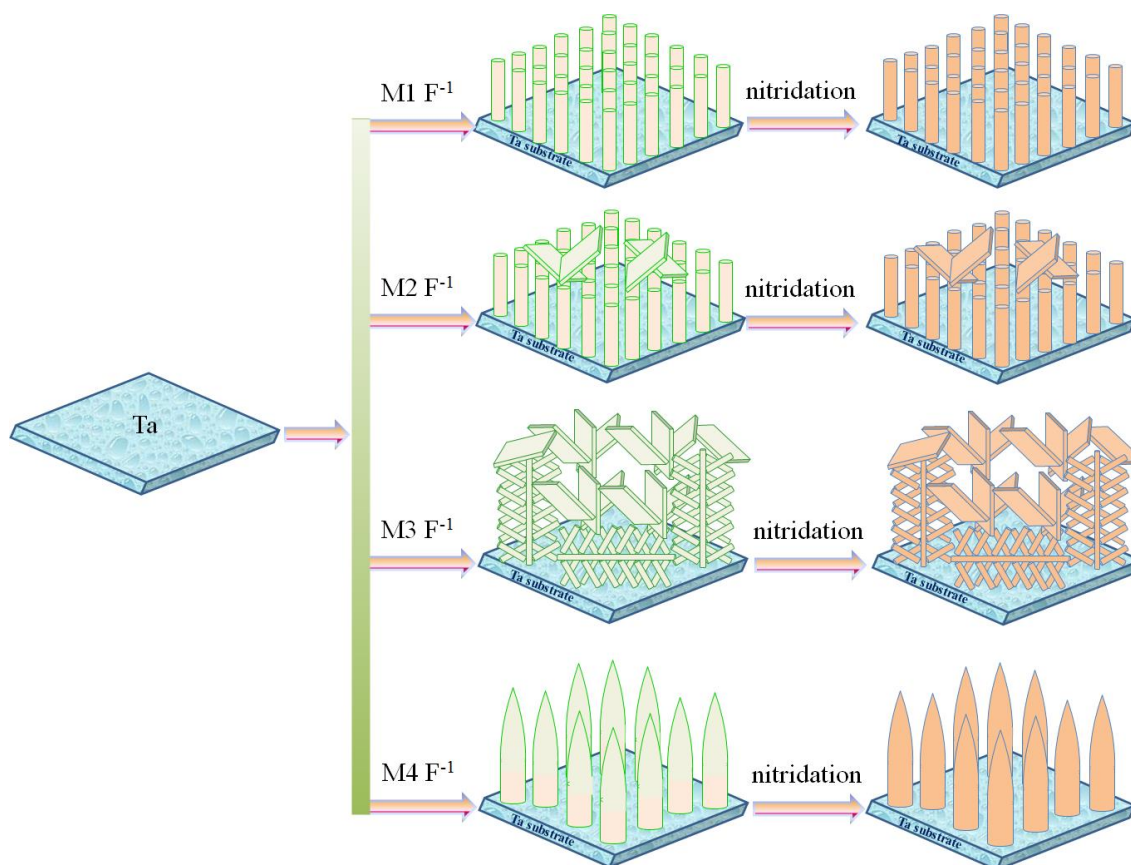


Figure S2. Schematic sketch of various-dimensional TaON arrays prepared the hydrothermal induced self-assembly technique with the increasing concentration of HF solution ($M1 < M2 < M3 < M4$).

As shown in Figure S2, the schematic sketch of shape-dependent F-Ta₂O₅ and TaON arrays using the increasing concentration of HF solution ($M1 < M2 < M3 < M4$). The relative low concentration of HF, the morphology and growth process has been presented for the F-Ta₂O₅ nanorod array prepared via the vapor-phase hydrothermal process in the mild HF environmental condition. Increasing a little amount of HF (M2) with the relative high vapor pressure, a small quantity of F-Ta₂O₅ nanosheets appeared on the surface of the F-Ta₂O₅ nanorod array. Especially, parts of nanorods and nanosheets were intercrossed each other. Under the use of HF solution (M3), the homogeneous nanosheet/nanorod-assembled flowers were achieved because it is sufficient to dissolve the Ta substrate by this HF concentration in the reaction zone. Particularly, the multilayered

photoanode with the nanosheet-like flowers (top layer) and nanorod-like caterpillars (underlayer) as the stack integration were formed on the surface of Ta substrate. Soaring to the highest concentration of HF solution (M4), the spindle-like F-Ta₂O₅ nanostructures were uniformly produced. Currently, it is noted that the white F-Ta₂O₅ thin film fragments were observed in the autoclave after the vapor-phase hydrothermal reaction, indicating the initial F-Ta₂O₅ film was peeled off the Ta substrate and then the spindle-like F-Ta₂O₅ array was grown again on the Ta substrate due to the high HF vapor pressure. Moreover, the dimension-dependent TaON arrays were fabricated by the subsequent nitridation with elaborate nitridation temperatures using the F-Ta₂O₅ arrays as raw materials. Thus, the comparison of the shape-dependent F-Ta₂O₅ and TaON arrays indicates that there is no obvious change upon the morphology before and after nitridation for the tantalum-based photoanode.

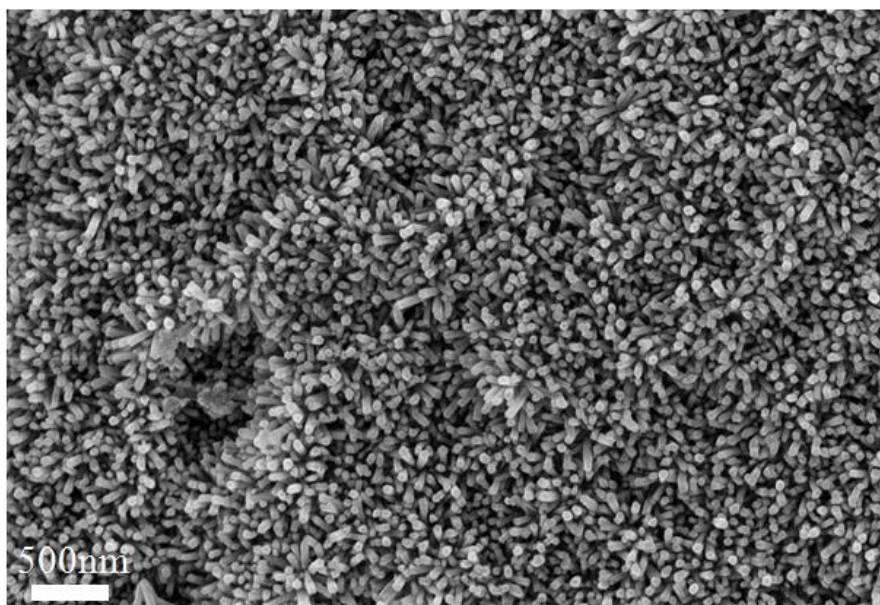


Figure S3. Typical magnified top-view scanning electron microscopy images of the nanorods-assembled TaON nanostructured array.

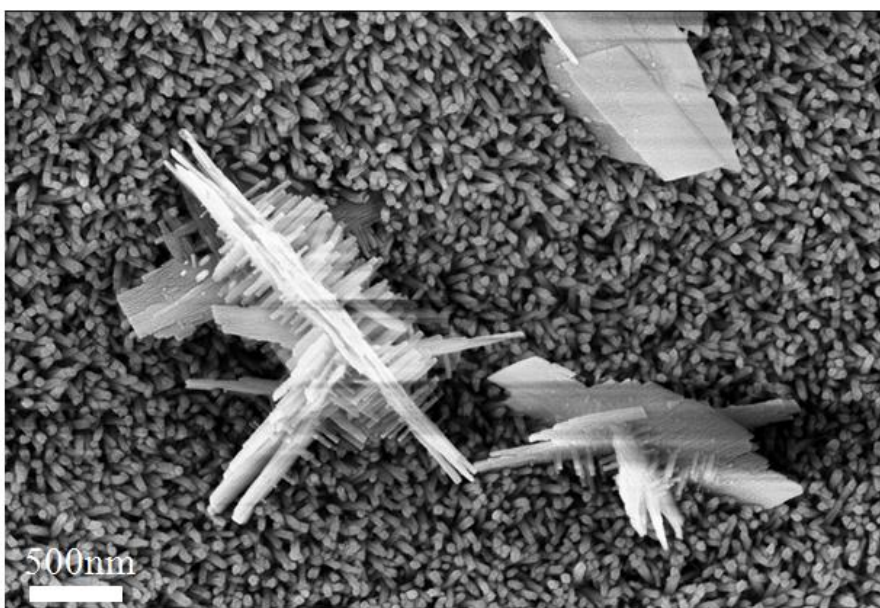


Figure S4. Typical magnified top-view scanning electron microscopy images of the nanorods-assembled TaON nanostructured array with a little content of nanosheets.



Figure S5. Typical magnified top-view scanning electron microscopy images of the 1D/2D nanorod/nanosheet-assembled TaON nanostructured array.

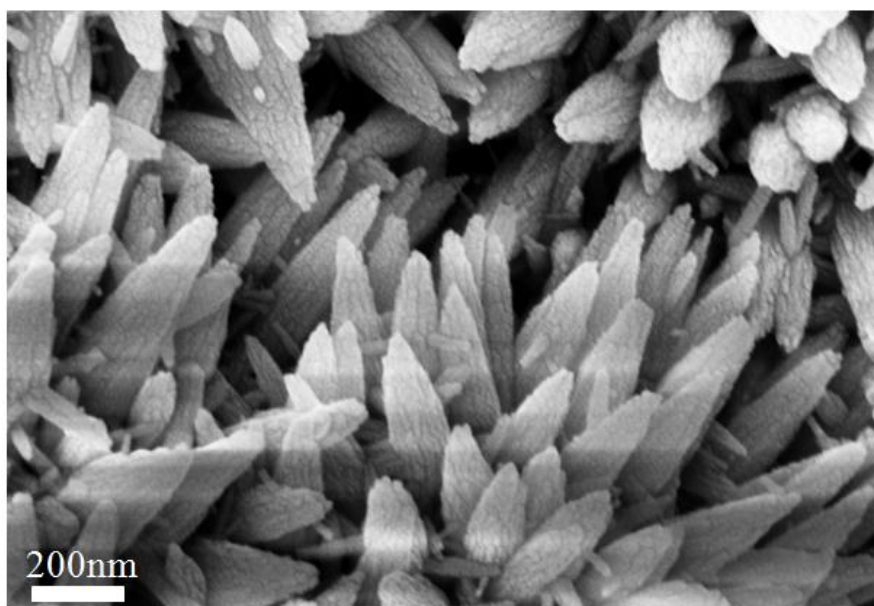


Figure S6. Typical magnified top-view scanning electron microscopy images of the one-dimensional spindle-assembled TaON nanostructured array.

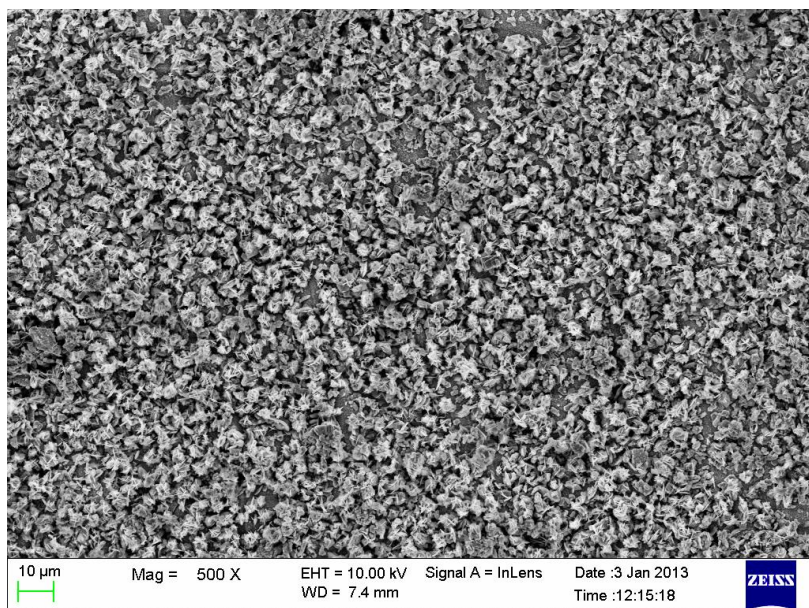


Figure S7. Typical top-view scanning electron microscopy images of the 1D/2D nanorod/nanosheet-assembled TaON nanostructured array.

In order to check the difference of various-dimensional F-Ta₂O₅ and TaON array, the magnified SEM images were presented in Figure 1. Especially, the large-scale nanosheets/nanorods-assembled TaON array with the high yields has presented in Figure S7. Thus, the comparison of the shape-dependent F-Ta₂O₅ and TaON arrays indicates that there is no obvious change upon the morphology before and after nitridation for the tantalum-based photoanode.

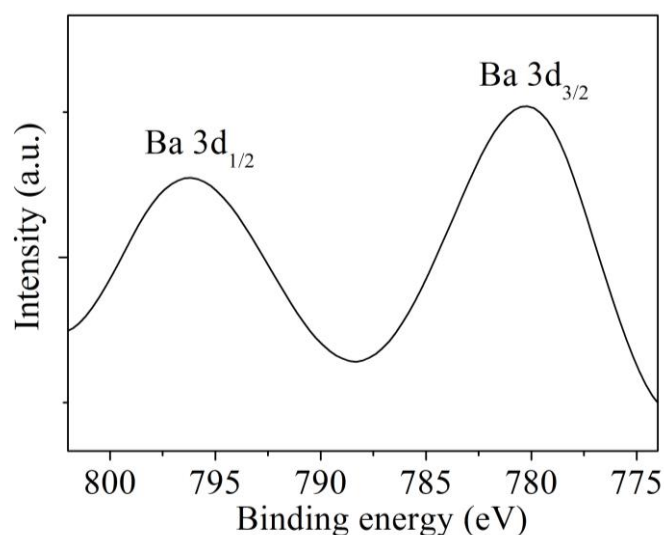


Figure S8. Ba 2p of X-ray photoelectron spectra of the three-dimensional nanosheets/nanorods assembled Ba-TaON nanostructured array.

According to the analysis of X-ray photoelectron spectra, the atomic ratios of N/Ta and O/Ta for the 1D/2D nanorod/nanosheet-assembled Ba-TaON nanostructured array were 1.2 and 0.9, respectively. Moreover, the Ba 2p of X-ray photoelectron spectra of the 1D/2D nanorod/nanosheet-assembled Ba-TaON nanostructured array has been incorporated in supporting information (Figure S8), indicating that Ba is uniformly distributed inside the film.

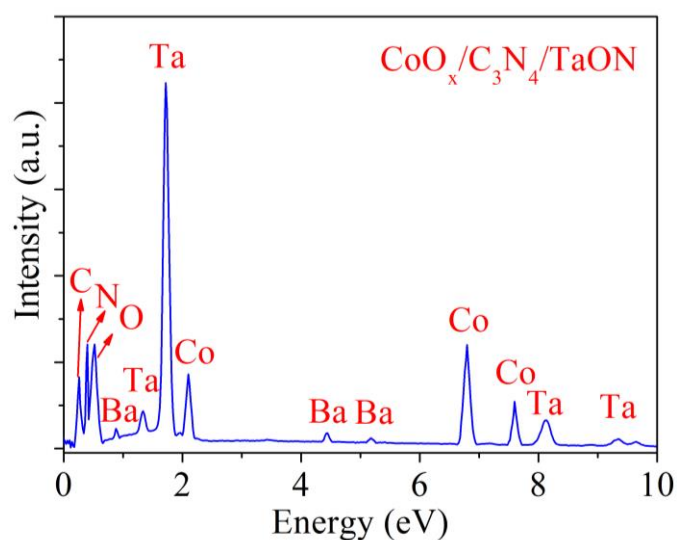


Figure S9. Energy-dispersive X-ray spectra of the CoO_x/C₃N₄/Ba-TaON heterostructured array.

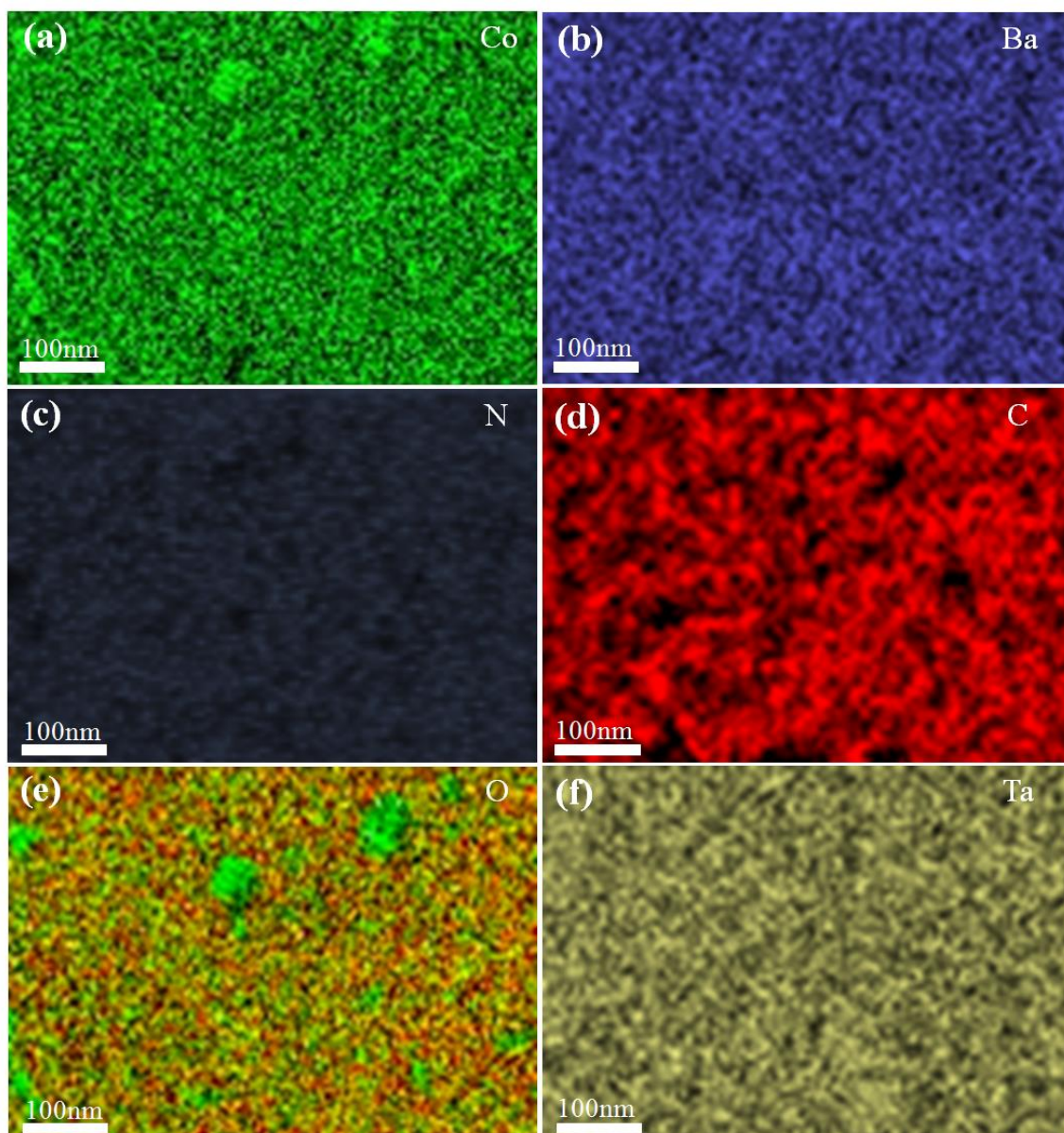


Figure S10. Energy-dispersive X-ray spectra of the $\text{CoO}_x/\text{C}_3\text{N}_4/\text{Ba-TaON}$ heterostructured array. (a) Co, (b) Ba, (c) N, (d) C, (e) O, (f) Ta, respectively. The elemental mapping revealed uniform distribution of Co, C, N, O, Ba, Ta elements of the $\text{CoO}_x/\text{C}_3\text{N}_4/\text{Ba-TaON}$ sample.

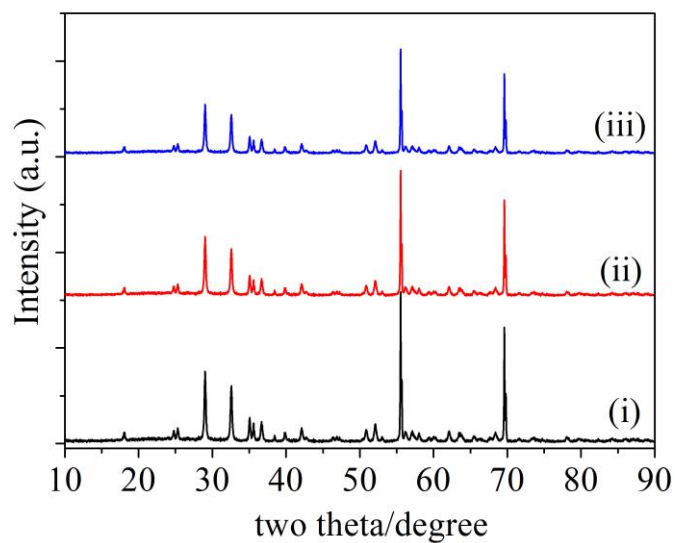


Figure S11. XRD patterns of the different photoanodes. (i) Ba-TaON, (ii) C₃N₄/Ba-TaON and (iii) CoO_x/C₃N₄/Ba-TaON arrays.

After Ba²⁺ doping into F-Ta₂O₅ array, the analysis of XRD patterns indicates both TaON and Ba-TaON through the elaborate nitridation, have the same crystal structure (Figure S11), which is in good agreement with the phenomenon of barium-doped Ta₃N₅.² Moreover, after the deposition of CoO_x nanoparticles and C₃N₄ nanosheets, the C₃N₄/Ba-TaON and CoO_x/C₃N₄/Ba-TaON arrays exhibit the same crystal structure as the Ba-TaON array, indicating that there is no obvious change upon the crystal structure for Ba-TaON, C₃N₄/Ba-TaON and CoO_x/C₃N₄/Ba-TaON arrays.

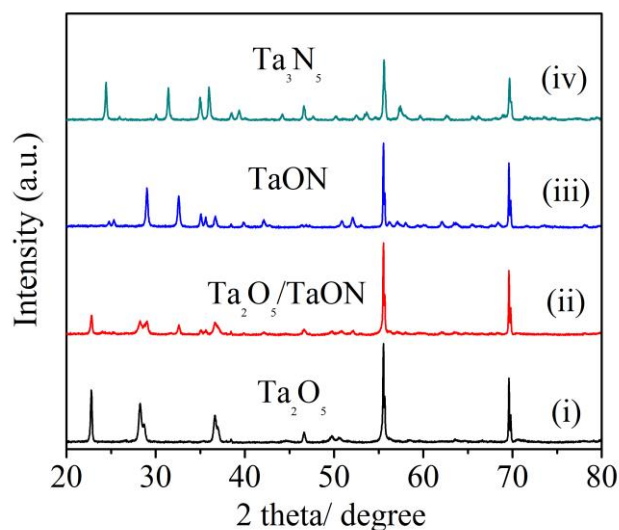


Figure S12. (a) XRD patterns of tantalum-based arrays with various nitridation temperature : (i) without nitridation, (ii) 650 °C, (iii) 700 °C and (iv) 750 °C. (b) Ta 4f XPS spectra of (i) TaON, (ii) C₃N₄/TaON and (iii) CoO_x/C₃N₄/TaON.

The XRD pattern of as-prepared product indicates that the sample consists of F-Ta₂O₅ arrays without nitridation, as shown in Figure S12. After the nitridation at 650 °C, the major phase is comprised of the mixture of Ta₂O₅/TaON arrays. With the increase of nitridation temperature up to around 700 °C, the single-phase TaON arrays were obtained. However, the F-Ta₂O₅ phase without nitridation was transformed into Ta₃N₅ phase under the nitridation of 750 °C. Thus, the nitridation temperature, plays a vital role in the formation of TaON arrays grown on the Ta substrate.

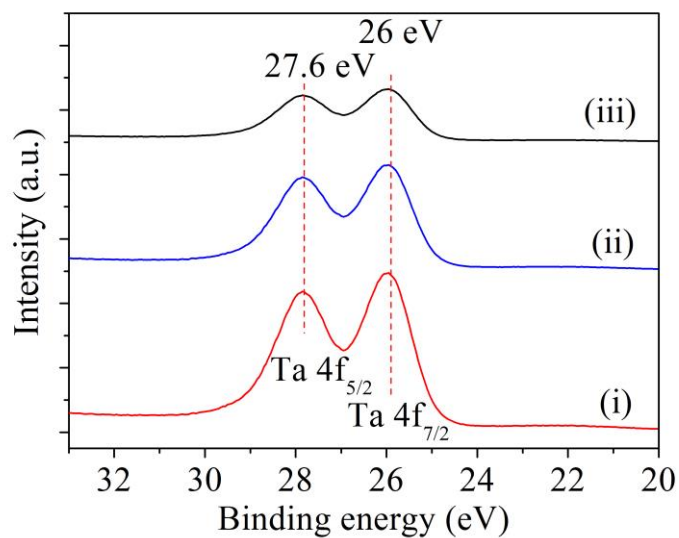


Figure S13. Ta 4f X-ray photoelectron spectra of (i) TaON, (ii) C₃N₄/TaON and (iii) CoO_x/C₃N₄/TaON.

Two distinct peaks at 26.0 (Ta 4f_{7/2}) and 27.6 eV (Ta 4f_{5/2}) in all samples are seen in the high-resolution Ta 4f spectrum.¹

Reference.

1. Y. Li, L. Zhang, A. Torres-Pardo, J. M. González-Calbet, Y. Ma, P. Oleynikov, O. Terasak, S. Asahina, M. Shima, D. Cha, L. Zhao, K. Takanabe, J. Kubota, K. Domen, Nat. Comm., 2013, 4, 2566.

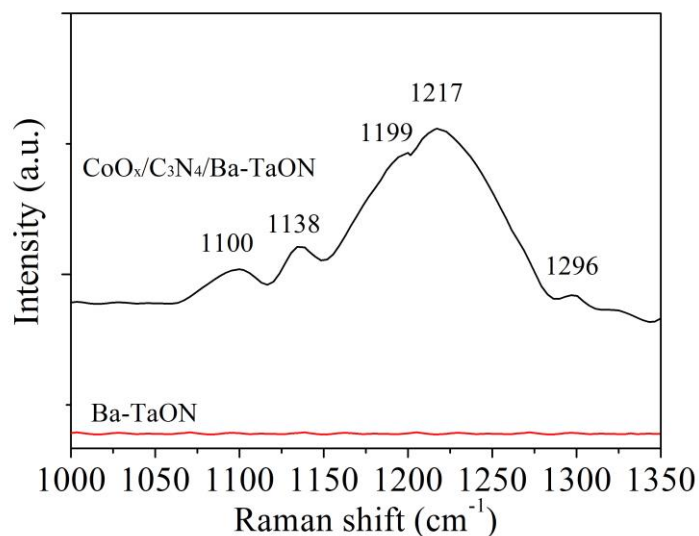


Figure S14. Raman spectra of nanosheet/nanorod-assembled Ba-TaON and CoO_x/C₃N₄/Ba-TaON heterostructured array.

Since the N peak in X-ray photoelectron spectra (XPS), as shown in Figure 5e, is not very convincing. Especially, the presence of N can be both due to graphitic nitrogen or N doping in the oxide, it is hard to come into a conclusion. Thus, we have provided the clear evidence of Raman analysis in CoO_x/C₃N₄/Ba-TaON heterostructured array. As shown in Figure S14, the Raman spectra of CoO_x/C₃N₄/Ba-TaON heterostructured array shows characteristic peaks around 1100, 1138, 1199 and 1217 cm⁻¹.¹ However, there is no any peak in the Ba-TaON array. The above-mentioned results from the analysis of X-ray photoelectron spectra (XPS) and Raman spectra confirmed the presence of C₃N₄ in the CoO_x/C₃N₄/Ba-TaON heterostructured array.

Reference.

1. Q. J. Xiang, J. G. Yu, M. Jaroniec, *J. Phys. Chem. C.*, 2011, 115, 7355.

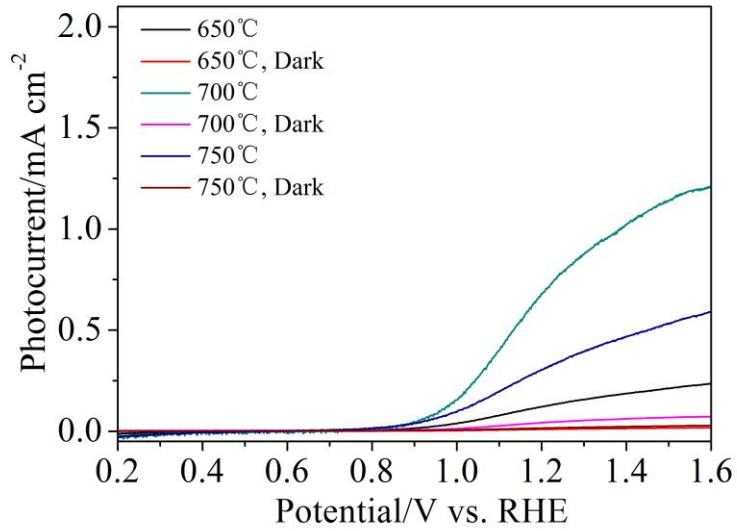


Figure S15. Photocurrent–potential curves under AM 1.5G-simulated sunlight of TaON photoanode under the nitridation of 650~750 °C.

Figure S15 shows the photocurrent density-potential curves dependent on the various samples under the nitridation temperature between 650 and 750 °C. At a certain nitridation temperature of 650, 700 and 750 °C, it is obvious that the difference of PEC performance is ascribed to the composition and the crystallinity of Ta-based arrays. As shown in Figure S15, the appropriate nitridation temperature for the TaON array is around 700 °C.

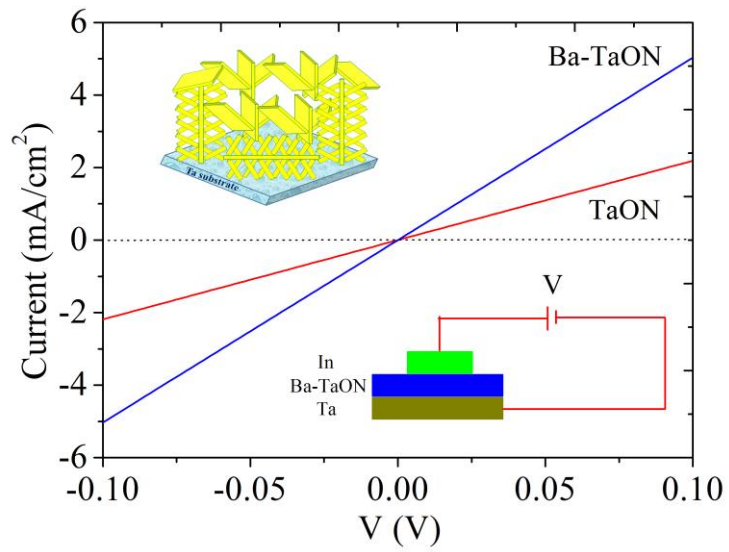


Figure S16. I-V curves of the photoelectrodes of the undoped and Ba-doped TaON arrays. Bottom-right inset shows the schematic drawing of the structure for I-V measurement. Indium thin film was evaporated on the surface through a shadow mask as top electrode.

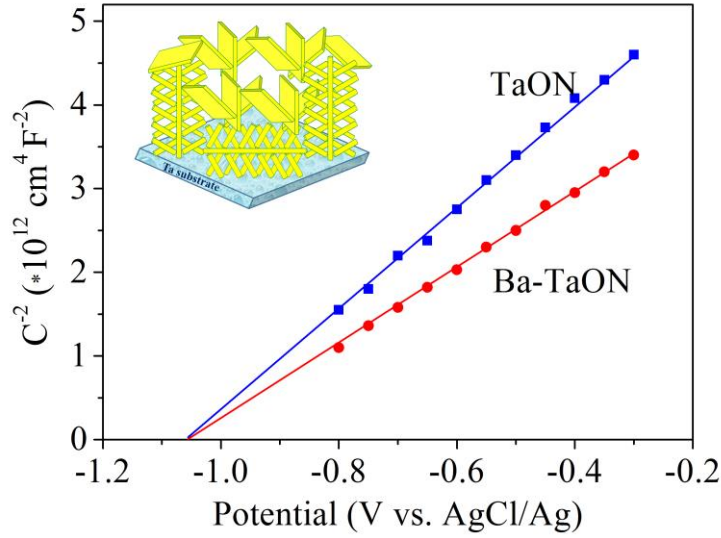


Figure S17. Mott–Schottky plots of TaON and barium-doped TaON photoelectrodes in 1.0 M NaOH solution (pH = 13.6) under the frequency of 3000 Hz.

Photoelectrodes were analyzed by electrochemical impedance spectroscopy. The Mott–Schottky plots of TaON and barium-doped TaON (Ba-TaON) photoelectrodes are shown in 1 M NaOH solution (pH = 13.6) at frequencies of 3000 Hz (Figure S17). In such an ideal case, linear Mott–Schottky plots (i.e., $1/C^2$ vs potential plots) can be obtained, and they supply information on the doping density and the flat band potential, V_{fb} , of the semiconductor. As shown in Figure S17, the Mott–Schottky plot of TaON and barium-doped TaON photoelectrodes has a slope that is consistent with the behavior of an n-type semiconductor. The flat band potential, V_{fb} , of TaON and Ba-TaON is approximated to be -1.05 V vs. Ag/AgCl at pH = 13.6.

The capacitance–potential measurements on TaON and Ba-TaON arrays are presented as a Mott–Schottky plot following the equation below:

$$\frac{1}{C^2} = \frac{2}{\varepsilon_0 \varepsilon N_A A^2} \left(V - V_{fb} - \frac{k_B T}{e} \right) \quad (1)$$

In eqn (1) above, C is the space-charge capacitance of the semiconductor; ε_0 is the permittivity in

vacuum, ϵ is the dielectric constant of TaON (taken as 24),¹ e is the electronic charge, V_{fb} is the flat-band potential, V is the applied potential, N_A is the number density of acceptors in TaON, T is the absolute temperature, A is area of the electrode and k_B is the Boltzmann constant. The flat band potential (V_{fb}) is determined (eqn (2) below) after the small thermal correction ($k_B T/e$) of the intercept (V_0) which is estimated from extrapolating the linear part of the curve to $1/C^2$ equals to zero on the potential axis.²

$$V_{fb} = V_0 + \frac{k_B T}{e} \quad (2)$$

The carrier density (N_A) was calculated from the slopes of the Mott–Schottky plots:

$$N_A = \frac{2}{\epsilon_0 \epsilon N_A A^2} \quad (3)$$

Accordingly, the value of carrier concentration estimated from the slope obtained from extrapolating the linear part of the curve to $1/C^2$ equals to zero on the potential axis at 3000 Hz frequency for TaON and Ba-TaON array were 1.60×10^{18} and $2.42 \times 10^{18} \text{ cm}^{-3}$, respectively. Thus, the resistance of the system can be accordingly reduced, leading into the photocurrent enhancement of Ba-TaON array photoelectrodes.

References.

1. X. Zou, J. P. Xu, X. F. Zhang, *Research & Progress of Solid State Electronics*, 2010, 30, 338.
2. L. C. Wang, N. R. de Tacconi, C. R. Chenthamarakshan, K. Rajeshwar and M. Tao, *Thin Solid Films*, 2007, 515, 3090.

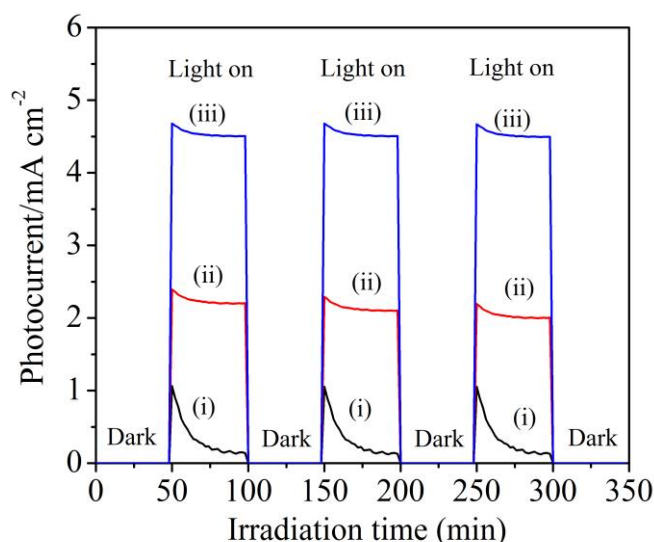


Figure S18. Transient photocurrent density versus time in 1 M NaOH solution of pH=13.6 under AM 1.5G irradiation at 1.23 V versus RHE for the different photoanodes. (i) Ba-TaON, (ii) C₃N₄/Ba-TaON and (iii) CoO_x/C₃N₄/Ba-TaON arrays.

It is well-known that the practical application of (oxy)nitrides photoelectrodes during water splitting reaction is hindered due to the poor photocurrent stability as the serious obstacle. After the enhancement of photocurrent through the hierarchical Ba-TaON array, the major aim of this work is to improve the photostability of hierarchical Ba-TaON photoelectrode. Compared with the photocurrent densities of Ba-TaON photoelectrode in NaOH (pH=13.6) solution at 1.23 V vs. RHE under AM 1.5G illumination (100 mW/cm²), the effect of CoO_x nanoparticles and C₃N₄ nanosheets on the photostability of Ba-TaON array was examined. As shown in Figure S16, the photocurrent generated by the bare Ba-TaON array decreases significantly within a short times, and the steady state photocurrent is negligibly low in few seconds, indicating that accumulation of photogenerated holes at the surface of Ba-TaON due to poor kinetics for water splitting and subsequent surface oxidative decomposition of Ba-TaON. As shown in Figure S18, the transient photocurrent density of the CoO_x/C₃N₄/Ba-TaON heterojunction was more than 4.45 mA/cm², whereas those of the

$\text{C}_3\text{N}_4/\text{Ba-TaON}$ photoanode and the Ba-TaON photoanode were less than 2.12 and 0.13 mA/cm^2 , respectively, exhibiting the significant enhancement of the stable PEC water splitting of the Ba-TaON photoanodes. Furthermore, the bias value of 1.23 V vs. RHE was applied to the hybrid, the transient photocurrents also exhibit good switching behaviour (Figure S18). This result demonstrated that the separation rate of photogenerated electron-hole pairs increased due to the heterojunction built between CoO_x nanoparticles, C_3N_4 nanosheets and Ba-TaON.

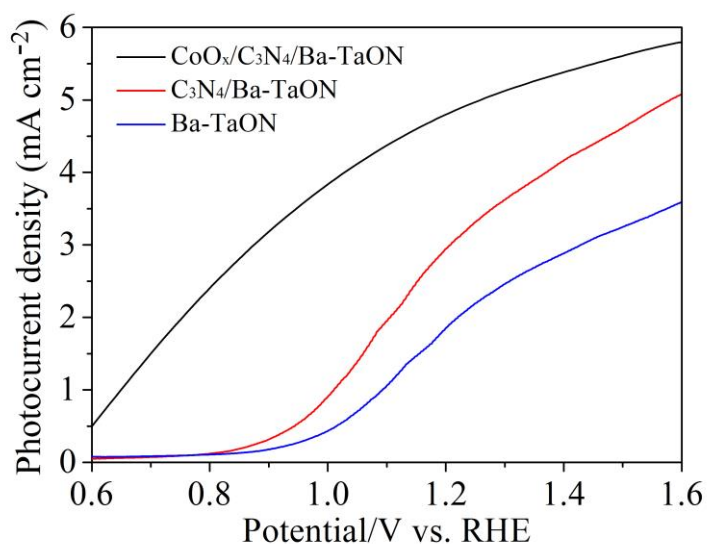


Figure S19. Photocurrent–potential curves under AM 1.5G-simulated sunlight of the hierarchical Ba-TaON, C₃N₄/Ba-TaON and CoO_x/C₃N₄/Ba-TaON photoanode with H₂O₂ as a hole-scavenging electrolyte under AM 1.5G simulated sunlight (100 mW/cm²).

To assess the effectiveness of this catalyst, an easily oxidized surrogate substrate was sought that would reveal the ultimate performance limit for these photoanodes in the absence of surface electron hole recombination.¹ For the sake of capturing holes into water oxidation more effectively, various sacrificial reductants,²⁻⁴ have been utilized in an attempt to maximally avoid surface recombination. In order to eliminate surface recombination by removing the transfer barrier, PEC H₂O₂ oxidation was shown to provide a useful metric for assessing the performance limits of the photoanodes.^{5,6} To quantify the contribution of $\eta_{\text{separation}}$ and η_{transfer} , the H₂O₂ is employed as a hole scavenger, which can be assumed that the surface recombination of charges is eliminated due to the rapid oxidation ($\eta_{\text{transfer}}=100\%$).⁷⁻⁹ The presence of H₂O₂ is employed to investigate the possible influence of surface recombination. Currently, the photoanode and the photocathode have been conducted in the separated reactors, eliminating the reductive pathway of H₂O₂ decomposition. Through the quantitative analysis, this work highlights the value of combining the advantages of

heteroepitaxy and surface modification to quantify the relative contribution of surface and bulk recombination.

The incident photon to current efficiency (IPCE) of these photoelectrodes is shown in Figure 5d. IPCE takes into account efficiencies for three fundamental processes which can be expressed by below Equation.⁹

$$IPCE = \eta_{absorbed} \times \eta_{separation} \times \eta_{transfer} \quad (1)$$

where $\eta_{absorbed}$ is the light harvesting efficiency, $\eta_{separation}$ is the separation efficiency for photogenerated carriers, and $\eta_{transfer}$ is interfacial charge transfer efficiency. In order to identify quantitative contribution of each parameter in above-mentioned Equation on the improved photocurrent, these processes should be investigated independently.

Since the rate of charge transfer to the electrolyte by oxidation of H_2O_2 at the semiconductor/electrolyte interface is very fast, it can be assumed that the surface recombination of charges is eliminated and $\eta_{transfer} \approx 100\%$ in the presence of H_2O_2 .⁷⁻¹³ The obtained photocurrent density (J_{H_2O} or $J_{H_2O_2}$) is thus defined as follows:

$$J_{H_2O} = J_{absorbed} \times \eta_{separation} \times \eta_{transfer} \quad (2)$$

$$\eta_{separation} = \frac{J_{H_2O}}{J_{absorbed}} \quad (3)$$

$$\eta_{transfer} = \frac{J_{H_2O}}{J_{H_2O_2}} \quad (4)$$

Especially, the band gap energy of 2.4 eV of the hierarchical TaON photoelectrode is consistent with the previous works.¹⁰⁻¹⁴ Based on all forementioned considerations, the photocurrent of 7.5 mA/cm² ($J_{absorbed}$) is theoretically possible under standard AM1.5 solar illustration.¹⁰⁻¹⁵

References.

1. D. K. Zhong, S. Choi, D. R. Gamelin, J. Am. Chem. Soc., 2011, 133, 18370.

2. H. Ye, J. Lee, J. S. Jang, A. J. Bard, *J. Phys. Chem. C*, 2010, 114, 13322.
3. M. P. Dare-Edwards, J. B. Goodenough, A. Hamnett, P. R. Trellick, *J. Chem. Soc., Faraday Trans. 1*, 1983, 79, 2027.
4. D. K. Zhong, S. Choi, D. R. Gamelin, *J. Am. Chem. Soc.* 2011, 133, 18370.
5. H. Dotan, K. Sivula, M. Grätzel, A. Rothschild, S. C. Warren, *Energy Environ. Sci.* 2011, 4, 958.
6. M. Zhou, J. Bao, W. T. Bi, Y. Q. Zeng, R. Zhu, M. S. Tao, Y. Xie, *ChemSusChem*, 2012, 5, 1420.
7. S. K. Pilli, T. E. Furtak, L. D. Brown, T. G. Deutsch, J. A. Turner, A. M. Herring, *Energy Environ. Sci.* 2011, 4, 5028.
8. D. K. Zhong, M. Cornuz, K. Sivula, M. Grätzel, D. R. Gamelin, *Energy Environ. Sci.* 2011, 4, 1759.
9. P. M. Rao, L. L. Cai, C. Liu, I. S. Cho, C. H. Lee, J. M. Weisse, P. D. Yang, X. L. Zheng, *Nano Lett.* 2014, 14, 1099–1105.
10. J. G. Hou, C. Yang, H. J. Cheng, S. Q. Jiao, O. Takeda and H. M. Zhu, *Energy Environ. Sci.*, 2014, 7, 3758–3768.
11. A. Suzuki, Y. Hirose, D. Oka, S. Nakao, T. Fukumura, S. Ishii, K. Sasa, H. Matsuzaki and T. Hasegawa, *Chem. Mater.*, 2014, 26, 976–981.
12. A. B. Murphy, P. R. F. Barnes, L. K. Randeniya, I. C. Plumb, I. E. Grey, M. D. Horne, J. A. Glasscock, *Int. J. Hydrogen Energy* 2006, 31, 1999–2017.
13. G. J. Liu, J. Y. Shi, F. X. Zhang, Z. Chen, J. F. Han, C. M. Ding, S. S. Chen, Z. L. Wang, H. X. Han, Can Li, *Angew. Chem. Int. Ed.* 2014, 53, 7295–7299.
14. C. Liu, N. P. Dasgupta, and P. D. Yang, *Chem. Mater.* 2014, 26, 415–422.
15. B. Klahr, S. Gimenez, F. Fabregat-Santiago, J. Bisquert, T. W. Hamann, *J. Am. Chem. Soc.* 2012, 134, 16693.